(Received 12 May 2025, Accepted 23 June 2025, Scheduled 8 July 2025)

Multi-Objective Optimization of an Asymmetric Segmented Less-Rare-Earth Permanent Magnet Motor

Lu Zhang[1, *], Jinbin Xu[2], and Chen Qi[2]

[1] *Yantai Vocational College, Department of Transportation Engineering, Yantai 264000, China*
[2] *Zibo Vocational Institute, Automotive Engineering College, Zibo 255000, China*

ABSTRACT: In order to reduce the use of rare-earth materials and solve the problem of rising manufacturing costs of permanent magnet motors due to higher rare-earth prices, this paper proposes an asymmetric segmented less-rare-earth permanent magnet motor (ASLREPMM), which combines NdFeB permanent magnets with ferrite permanent magnets to form a common excitation source. In order to efficiently design the parameters of this motor, an optimization strategy of sensitivity stratification and multi-objective optimization is proposed, with output torque, torque pulsation, cogging torque, and peak air-gap magnet density as the optimization objectives, and multi-objective optimization is carried out on the optimization variables with high sensitivity. Compared with the V-type permanent magnet motor (V-type PMM), the cogging torque of the optimized ASLREPMM is decreased by 49.67%, torque pulsation decreased by 10.77%, peak air-gap magnetic density increased by 0.051T, and the total amount of NdFeB material decreased by 2184 mm^3. The reasonableness of the structural design and the effectiveness of the optimization of the ASLREPMM are verified through experiments.

1. INTRODUCTION

In order to cope with the problems of global warming and depletion of fossil energy, the development of electric vehicles has become an important direction for the transformation of the automotive industry [1–3]. Permanent magnet motors are used in a large number of electric vehicles due to their advantages of high efficiency, high reliability, and high power density [4–7]. However, rare earth materials are non-renewable resources, and the production cost of permanent magnet motors used in electric vehicles has risen due to the increase in the price of rare earth materials [8–10]. In order to cope with this phenomenon, how to maintain the performance of permanent magnet motors and reduce the use of rare earth materials has become a hot spot of motor research nowadays.

Many scholars have performed research for less rare earth permanent magnet motors. Ref. [11] proposes a motor structure in which spoke-type NdFeB permanent magnets are connected in series with flat-type ferrite as the excitation source, which makes the motor torque pulsation smaller and the torque output smoother. Ref. [12] proposes a motor structure in which a double-layer NdFeB permanent magnet is placed in contact with a ferrite permanent magnet and adds magnet barriers on both sides of the magnetic poles, which results in the enhancement of the sinusoidal nature of the air-gap magnetic density waveform of the motor. Ref. [13] proposes a motor structure in which ferrite is added to the outer end of one side of the V-type permanent magnet, and a nonuniform air gap is added to the outer circle of the rotor core, which results in a reduction of the motor cogging torque and a reduction in the use of NdFeB permanent magnets. Ref. [14] proposes a motor structure in which symmetrically distributed ferrite is added to the inner end of the V-type permanent magnet so that the two types of permanent magnets form a parallel excitation, which results in an increase in the sinusoidal nature of the motor's reaction potential waveform and a decrease in the cogging torque. Ref. [15] proposes a motor structure in which a single-sided NdFeB permanent magnet and a single-sided ferrite of the same pole are co-excited, and a magnetic barrier is added to the ferrite side, which improves the weak magnetic speed expansion performance of the motor. Ref. [16] proposes a motor structure using only Alnico material to form V-shaped poles. The motor structure is arranged in such a way that the poles are in contact with each other at both ends, making the motor coreless, reducing the armature reaction and increasing the torque density. Ref. [17] proposes a motor structure in which a zigzag NdFeB permanent magnet is co-excited with a V-type ferrite permanent magnet, which adopts an asymmetric structure design and increases the output torque of the motor through the principle of reluctance torque.

The current research mainly focuses on proposing a reasonable motor structure without systematic optimization, and the excessive use of ferrite will affect the structural strength and processing difficulty of the motor. Aiming at the above problems, this paper proposes an asymmetric segmented less-rare-earth permanent magnet motor, which can reduce the cogging torque and torque pulsation of the motor, improve the sinusoidal nature of the air-gap magnetic density waveform, and enhance the performance of the rare-earth permanent magnet motor through the optimal design of the system while reducing the use of rare-earth materials to lower the cost of the motor. Finally, a prototype is fabricated, and an experimental platform is built for verification.

* Corresponding author: Lu Zhang (1979289259@qq.com).

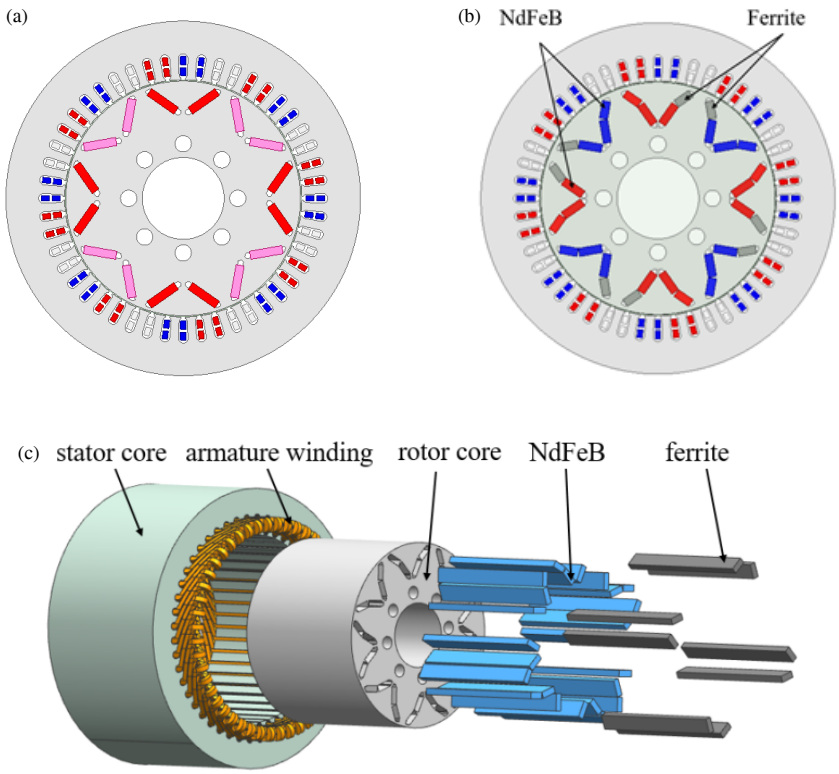

FIGURE 1. Comparison of motor structure. (a) Structure of V-type PMM. (b) Structure of ASLREPMM. (c) Exploded view of ASLREPMM.

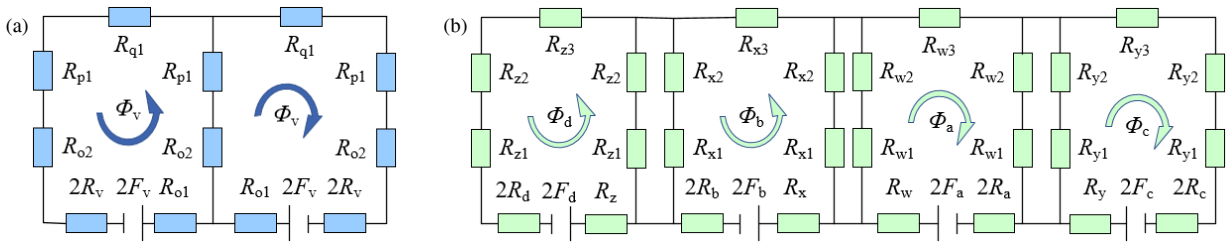

FIGURE 2. Different equivalent flux magnetic circuit distributions of the two motors. (a) Magnetic circuit diagram of V-type PMM. (b) Magnetic circuit diagram of ASLREPMM.

2. MOTOR STRUCTURE AND OPTIMIZATION ANALYSIS

2.1. Motor Topology and Parameters

Taking the V-type permanent magnet motor (V-type PMM) with only NdFeB permanent magnets as a reference, the motor structure diagram is shown in Fig. 1(a), and the ASLREPMM is proposed, as shown in Fig. 1(b). The ASLREPMM adopts 8-pole and 48-slot pole-slot coordination and distributed winding design scheme, and the rotor magnetic field is provided by the two permanent magnet materials of NdFeB and ferrite together. The exploded motor structure diagram is shown in Fig. 1(c).

The main flux paths of the V-type PMM and ASLREPMM are analyzed respectively, and different equivalent flux path distributions of the two motors are obtained as shown in Fig. 2.

In Fig. 2(a), F_v is the V-type permanent magnet magnet potential; R_v is the permanent magnet reluctance; R_o, R_p, and

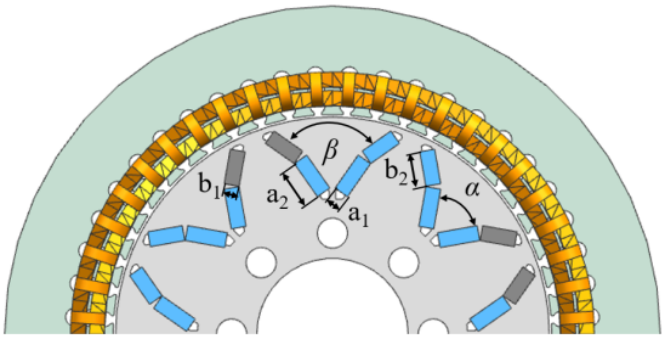

FIGURE 3. Motor structure topology.

R_q represent the reluctance of the magnetic flux as it passes through the rotor core, the air-gap reluctance, and the stator reluctance, respectively; and Φ_v is the effective flux of a flux loop. From Fig. 2(a), it can be seen that a symmetrical pole structure is formed because the V-type PMM is excited by a single excitation source, and the left and right magnetic poten-

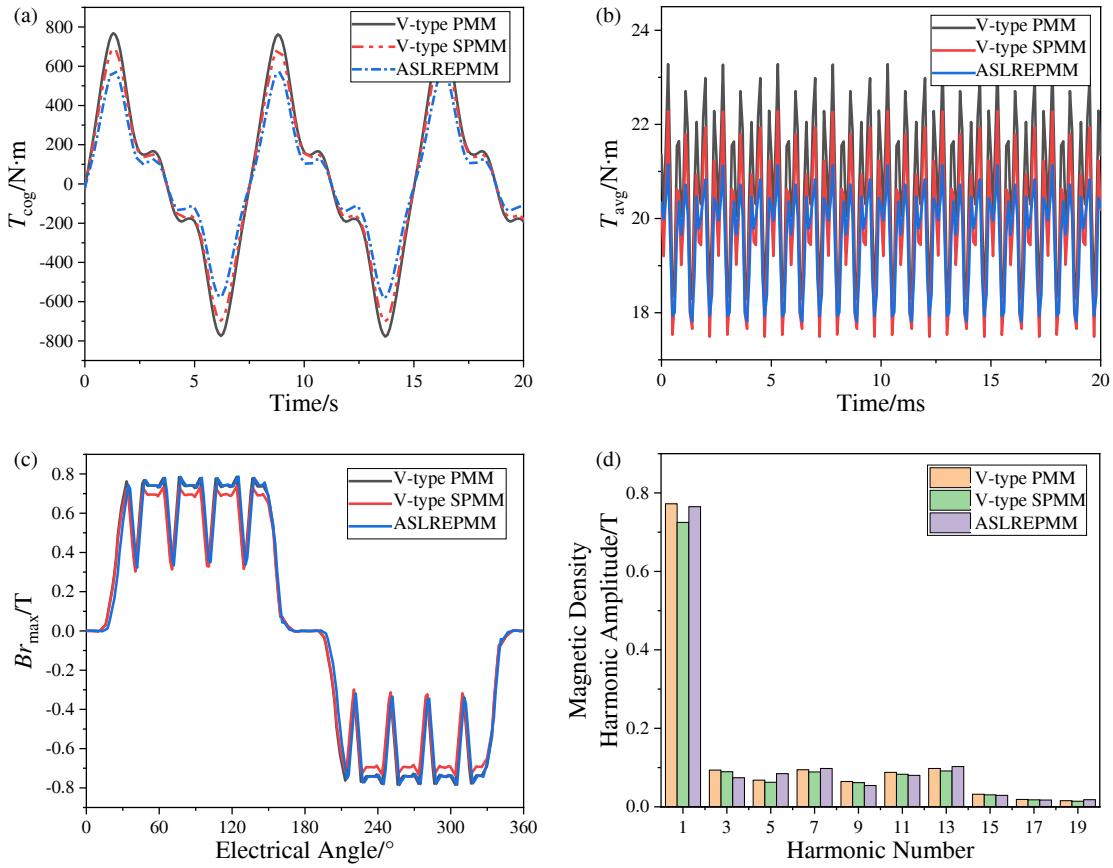

FIGURE 4. Comparison results. (a) Comparison chart of cogging torque. (b) Output torque comparison chart. (c) Comparison of air-gap magnetic density waveforms. (d) Comparison of magnetic density harmonic.

tials within the same pole are equal. In Fig. 2(b), F_a is the magnetic kinetic potential of the ferrite permanent magnet; F_b, F_c, and F_d are the magnetic kinetic potentials of the NdFeB permanent magnet; R_a is the magnetoresistance of the ferrite permanent magnet; R_b, R_c, and R_d are the magnetoresistance of the NdFeB permanent magnet; R_w, R_x, R_y, and R_z are the magnetoresistance of the respective magnetic flux circuits; and Φ_a, Φ_b, Φ_c, and Φ_d are the effective fluxes in the respective flux circuits. As can be seen from Fig. 2(b), the ASLREPMM consists of NdFeB permanent magnets and ferrite permanent magnets forming a parallel magnetic circuit for co-excitation, and the difference in the magnetomotive force between the left and right sides within the same pole is larger due to the different materials of the left and right sides of the permanent magnets within the same pole, which results in an asymmetric pole structure.

In order to make the two types of permanent magnets have a more flexible way of combining pole sizes, the NdFeB permanent magnets and ferrite permanent magnets inside the same pole are designed in segments. The topology of the motor structure is shown in Fig. 3. The inner end permanent magnet adopts a V-type arrangement with a small angle to achieve the magnetic aggregation effect, and the outer end permanent magnet adopts a V-type arrangement with a large angle to improve the sinusoidal nature of the air-gap magnetic density waveform, wherein the inner end V-type permanent magnet angle α and dimensions are not equal to the outer end V-type permanent magnet angle β and dimensions, and in the outer end V-type permanent magnet, the dimensions of the NdFeB permanent magnet are the same as those of the ferrite permanent magnet.

To ensure that the proposed ASLREPMM is comparable to the traditional V-type PMM, the two motors adopt the same stator and rotor size parameters and winding arrangement methods. According to the operating conditions and performance requirements of electric vehicles, the dimensional parameters and performance indicators of V-type PMM and ASLREPMM are shown in Table 1.

To further validate the optimization effect of asymmetric segmented structures on motor performance, this paper compares the electromagnetic characteristics of V-type permanent magnet motor and V-type segmented permanent magnet motor (V-type SPMM) that use NdFeB as the excitation source with those of ASLREPMM that use NdFeb and Ferrite as a mixed excitation source. The results are shown in Fig. 4.

As shown in Fig. 4, the ASLREPMM using NdFeB and Ferrite as a mixed excitation source exhibits smaller cogging torque and torque ripple, higher peak air gap magnetic flux density, better sinusoidal air gap magnetic flux density waveform, and lower high-order harmonic amplitudes. The results indicate that the asymmetric segmented pole structure achieves good optimization effects.

TABLE 1. Dimensional parameters and performance indicators of the two motors.

Name	Parametric
Stator Outer diamete/mm	130.0
Stator inner diameter/mm	87.0
Rotor outer diameter/mm	86.0
polar logarithm	4.0
Number of stator slots	48.0
Axial length/mm	70.0
rated speed/rpm	3000
Rated torque/N·m	19.0
rating/Kw	5.0
V-shaped permanent magnet width/mm	12.0
Thickness of V-shaped permanent magnet/mm	3.0
V-type permanent magnet clamping angle/°	110.0
Width of V-shaped permanent magnet at outer end/mm	7.0
Thickness of outer V-shaped permanent magnet/mm	3.0
Outer end V-type permanent magnet clamping angle/°	110.0
Width of V-shaped permanent magnet at inner end/mm	8.0
Thickness of V-shaped permanent magnet at inner end/mm	3.0
Inside end V-type permanent magnet clamping angle/°	70.0

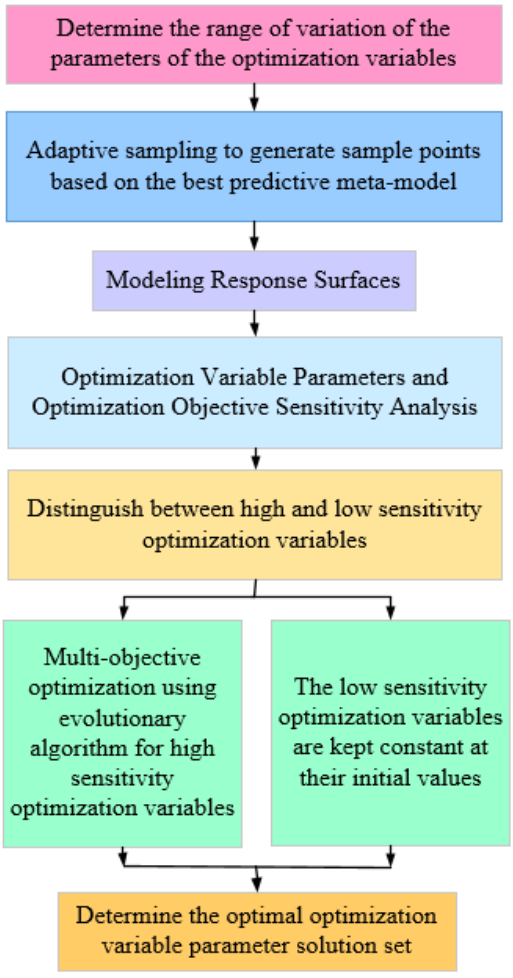

FIGURE 5. Sensitivity analysis flowchart.

2.2. Sensitivity Analysis and Multi-Objective Optimization

The initial design of the motor model is not the optimal model, and the connection between the optimization variables and the degree of influence on the optimization target is complex and variable. In order to reduce the optimization analysis time and improve the efficiency, the comprehensive sensitivity analysis is used to determine the optimization variables that have a high sensitivity influence on the optimization target, and the evolutionary algorithm is used to carry out multi-objective optimization for the optimization variables with a high sensitivity, to determine the best set of optimization variable solutions. The sensitivity analysis flowchart is shown in Fig. 5.

As can be seen from the analysis in Fig. 2, the number of permanent magnets used inside the magnetic poles and the angle between them can affect the performance of the motor. Therefore, based on the motor size parameters in Table 1, the range of variation of the optimization variable parameters is set as in Table 2.

TABLE 2. Optimization variable parameter variation ranges.

Optimization variable parameter	variation range
a_1/mm	2.5–3.0
a_2/mm	6.0–8.5
α/°	60.0–80.0
b_1/mm	2.5–3.0
b_2/mm	5.0–7.0
β/°	80.0–130.0

The motor is a drive motor, and the size and stability of the motor's output torque is an important index for evaluating the performance of the motor. In order to reduce the vibration and

TABLE 3. Selected sample sites.

Serial number	a_1/mm	a_2/mm	α/°	b_1/mm	b_2/mm	β/°	T_{avg}/N·m	$Br_{\max}$/T	T_{cog}/N·m	T_{pkavg}
1	2.54	6.07	79.44	2.54	6.28	114.72	14.94	0.391	0.229	0.233
2	2.51	7.04	71.67	2.82	5.72	128.61	13.98	0.375	0.159	0.190
3	2.82	6.90	69.44	2.96	6.06	123.06	14.94	0.419	0.208	0.191
4	2.90	7.46	72.78	2.99	6.94	103.61	19.32	0.765	0.504	0.158
5	2.68	7.74	76.11	2.63	6.72	81.39	20.82	0.927	0.863	0.392
...	...	...	...	...	...	...	...	...	...	...
46	2.80	7.64	75.63	2.89	6.69	119.06	17.75	0.671	0.610	0.239
47	2.70	7.33	73.13	2.92	6.19	87.81	18.12	0.716	0.463	0.266
48	2.86	6.23	74.38	2.86	6.31	115.94	15.32	0.409	0.216	0.213
49	2.67	6.55	70.63	2.55	6.94	112.81	16.59	0.509	0.425	0.329
50	2.89	8.42	71.88	2.61	5.31	109.69	16.53	0.626	0.126	0.116

TABLE 4. Values of sensitivity between each optimization variable and the optimization objective.

Parameters	β	b_2	b_1	α	a_2	a_1
T_{avg}	-0.41	0.66	0.04	0.25	0.57	0.06
$Br_{\max}$	-0.4	0.51	0.04	0.26	0.71	0.03
T_{cog}	-0.24	0.57	-0.07	0.19	0.3	0.03
T_{pkavg}	-0.39	0.31	-0.14	-0.03	-0.28	-0.06

noise during the driving process of the electric vehicle, the influence of the cogging torque on the motor performance should be considered in particular. Reducing leakage magnetic flux and improving the peak value of air-gap magnetic flux density and the sinusoidal nature of the waveform are issues that cannot be ignored in motor design.

Therefore, taking the cogging torque T_{cog}, output torque T_{avg}, torque ripple T_{pkavg}, and the peak flux density $Br_{\max}$ of the air gap as the optimization objectives, the sensitivity relationship between each optimization variable and the optimization objectives is analyzed. The motor optimization model is:

$$\begin{cases} \max T_{avg}(x_1, x_2, \ldots x_n) \\ \min T_{pkavg}(x_1, x_2, \ldots x_n) \\ \min T_{cog}(x_1, x_2, \ldots x_n) \\ \max Br_{\max}(x_1, x_2, \ldots x_n) \end{cases} \tag{1}$$

Based on the optimization variable constraints set in Table 2 and the reference V-type PMM, in this optimization model, the motor output torque should be set to a larger value. The torque ripple should be set to a smaller value. The cogging torque should be set to a smaller value. The air-gap magnetic flux density should be set to a larger value.

According to the range of values of the optimization variables determined above to carry out sensitivity analysis of each optimization variable, but due to the optimization of six variables, even if each variable in the range of only five values, the sampling point is as high as 15625. In order to simplify the process of the selection of the sampling point and the number of sampling points, the best predictive meta-model adaptive sampling method is used to select the sample points, and the value of the sample point is taken as 50. Some of the sample points are shown in Table 3.

The contour plots between some of the optimization variables and the optimization objectives are shown in Fig. 6.

As can be seen from Fig. 6, the degree and direction of the influence of each optimization variable on the optimization objective are different, and the relationship between each optimization variable and the optimization objective is not a simple linear relationship. The combination of multiple optimization variables and the assignment of weights to multiple optimization objectives make the optimal set of parameter solutions exist in the optimization variables.

The results of the sensitivity analysis and the sensitivity values between each optimization variable and the optimization objective are shown in Fig. 7 and Table 4, respectively.

From Fig. 7 and Table 4, it can be seen that the degree and direction of the influence of each optimization variable on the optimization objective are different, and the thicknesses of the V-type permanent magnets at both the inner and outer ends have a small influence on the motor's various performance indexes. Both the angle and width of the outer V-type permanent magnets have the greatest influence on the output torque, and there is a negative and positive correlation between these two optimization variables and the motor performance indicators, respectively. Both the angle and width of the inner V-type permanent magnets have the greatest influence on the peak air gap density, and both are negatively correlated with torque pulsation and positively correlated with other performance indicators.

In order to distinguish the set of optimization variables that have a higher sensitivity to the optimization objective, weights

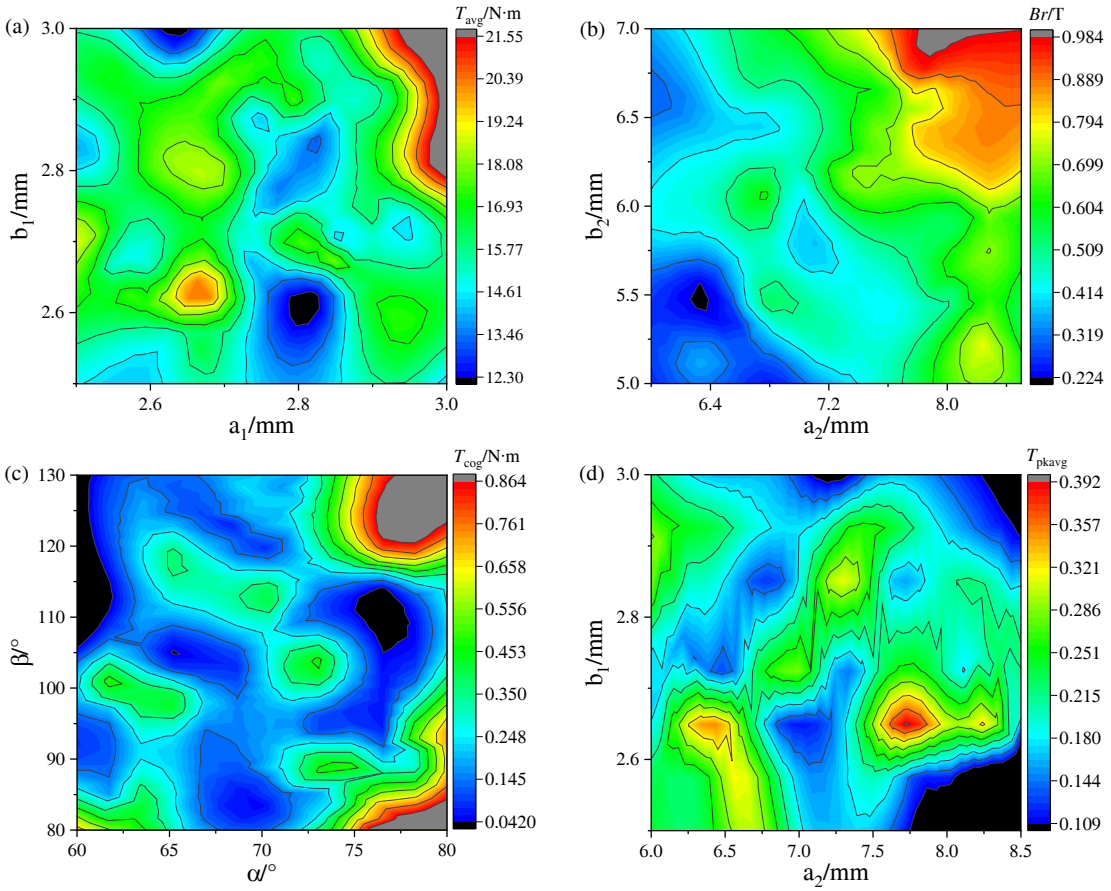

FIGURE 6. Contour plots of some of the optimization variables against the optimization objective. (a) a_1, b_1 and T_{avg}. (b) a_2, b_2 and $Br_{\max}$. (c) α, β and T_{cog}. (d) a_2, b_1 and T_{pkavg}.

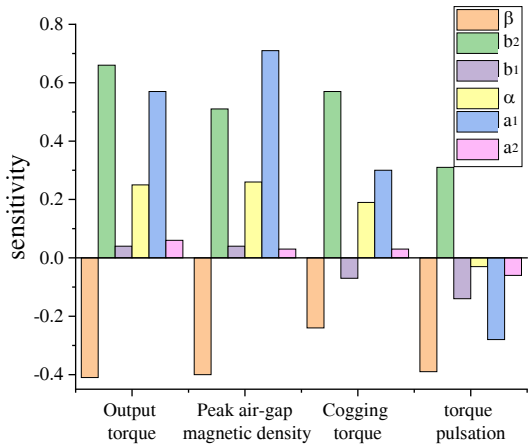

FIGURE 7. Results of sensitivity analysis.

are assigned to each optimization objective. Since the motor is used as a drive motor for electric vehicles, the weights of output torque and torque pulsation are assigned 0.25 respectively, and since the high harmonics of the air-gap magnetism and the sinusoidal nature of the waveform can affect the size of the cogging torque, the weight of the air-gap magnetism is assigned 0.3 and that of the cogging torque assigned 0.2. The comprehensive sensitivity of each optimization variable is calculated as:

$$S(x_i)=\lambda_1|G_1(x_i)|+\lambda_2|G_2(x_i)|+\lambda_3|G_3(x_i)|+\lambda_4|G_4(x_i)| \quad (2)$$

where $S(x_i)$ is the Comprehensive sensitivity of the optimization variables; λ_1 is the weighting coefficient of the output torque; $|G_1(x_i)|$ is the absolute value of the sensitivity of an optimization variable to the output torque; λ_2 is the weighting coefficient of the torque pulsation; $|G_2(x_i)|$ is the absolute value of the sensitivity of an optimization variable to the torque pulsation; λ_3 is the weighting coefficient of the peak airgap magnetic density; $|G_3(x_i)|$ is the absolute value of the sensitivity of an optimization variable is the absolute value of sensitivity to peak air gap density; λ_4 is the weighting coefficient of cogging torque; $|G_4(x_i)|$ is the absolute value of sensitivity to cogging torque for a particular optimization variable.

The comprehensive sensitivity of each optimization variable to the optimization objective is calculated in Table 5.

The comprehensive sensitivity of each optimization variable is defined as high sensitivity optimization variable if it is greater than 0.15 and vice versa for low sensitivity optimization variable. The high sensitivity optimization variables were identified as the angle β of the outer V-type permanent magnet, the width b_2 of the outer V-type permanent magnet, the angle α of the inner V-type permanent magnet and the width a_2 of the inner V-type permanent magnet, and the low sensitivity optimization variables were the thickness b_1 of the outer V-type permanent magnet and the thickness a_1 of the inner V-type permanent magnet.

TABLE 5. Comprehensive sensitivity of the optimization variables.

optimization variable	β	b_2	b_1	α	a_2	a_1
Comprehensive sensitivity	0.368	0.5095	0.043	0.186	0.4855	0.033

While keeping the thickness b_1 of the outer end V-type permanent magnet and the thickness a_1 of the inner end V-type permanent magnet as 3.0 mm, respectively, according to the determined high sensitivity optimization variables, the number of sampling points is set to 200, and the evolutionary algorithm is used to perform multi-objective optimization of the high sensitivity optimization variables.

Evolutionary algorithms classify sample populations according to non-dominance ordering operators, use cross-breeding and continuous mutation to generate new populations, and search for optimal solutions while preserving the superior factors of the parent generation.

The formula for calculating the binary cross-selection operator is as follows:

$$\begin{cases} x_{1,n+1} = 0.5 \times [(1-\varphi_1)x_{1,n} + (1+\varphi_1)x_{2,n}] \\ x_{2,n+1} = 0.5 \times [(1+\varphi_1)x_{1,n} + (1-\varphi_1)x_{2,n}] \end{cases} \tag{3}$$

In the formula, $x_{1,n}$ and $x_{2,n+1}$ are the parent individuals in the initial population; $x_{1,n+1}$ and $x_{2,n+1}$ are the offspring individuals generated by crossover; φ_1 is the uniform factor.

The formula for calculating the uniform factor is as follows:

$$\varphi_1 = \begin{cases} (2\beta_1)^{\frac{1}{\sigma_1+1}} & \beta_1 \le 0.5 \\ (2-2\beta_1)^{\frac{1}{\sigma_1+1}} & \beta_1 > 0.5 \end{cases} \tag{4}$$

In the formula, β_1 is a random number between 0 and 1; σ_1 is the cross distribution index.

The formula for selecting the mutation operator is as follows:

$$\begin{aligned} x_{n+1} &= x_n + \varphi_2(x_n^{\max} - x_n^{\min}) \\ \varphi_2 &= \begin{cases} (2\beta_2)^{\frac{1}{\sigma_2+1}} & \beta_2 \le 0.5 \\ 1-(2-2\beta_2)^{\frac{1}{\sigma_2+1}} & \beta_2 > 0.5 \end{cases} \end{aligned} \tag{5}$$

In the formula, x_n is the selected parent individual; x_{n+1} is the offspring individual generated by crossover mutation; $x_n^{\max}$ is the maximum value of the optimization variable; $x_n^{\min}$ is the minimum value of the optimization variable; φ_2 is the mutation coefficient; β_2 is a random number between 0 and 1; σ_2 is the mutation distribution index.

According to the calculation of the above equation, evolutionary algorithm parameters are set as follows: initial population size is 20; final population size is 200; maximum number of evolutionary generations for the operator is 25; stopping number of evolutionary generations is 20; final archiving number of generations is 20; and number of parent individuals is 20. Among them, simulated binary crossover is used to uniformly select the operator, with a crossover probability of 50% and a distribution index of 0.2. The results of the mutation operator selection follow a normal distribution. A sorting algorithm is used to compare the two operators and select the optimal one. When the evolutionary algorithm performs multi-objective optimization, the initial standard deviation is 0.05, and the final standard deviation is 0.01. The final results are displayed using a Pareto distribution surface.

Under the combined consideration of multiple optimization objectives, the Pareto frontier distribution graph containing the solution set of high sensitivity optimization variables is obtained, as shown in Fig. 8.

In Fig. 8, the black dots represent the set of solutions to the optimization variables that make up the Pareto frontier surface, and the red dots represent the set of solutions to the optimization variables that do not meet the constraints. As can be seen from Fig. 8, the selection of different optimization variable solution sets affects the optimization objectives to different degrees, and the enhancement of the effectiveness of a single optimization objective may lead to a decrease in the effectiveness of other optimization objectives. In order to improve the performance of the motor as a whole, the solution set of 49 groups of optimization variables identified in the Pareto frontier surface is preferred according to the weight coefficients of each optimization objective determined in the previous section and the performance index of the V-type permanent magnet motor used as a reference, and the solution set parameter preference formula is as follows:

$$\begin{aligned} &Y(d_i) = \\ &\lambda_1 \frac{T_{avg}(d_i) - T_{avg}(d_0)}{T_{avg}(d_0)} - \lambda_2 \frac{T_{pkavg}(d_i) - T_{pkavg}(d_0)}{T_{pkavg}(d_0)} \\ &+\lambda_3 \frac{Br_{\max}(d_i) - Br_{\max}(d_0)}{Br_{\max}(d_0)} - \lambda_4 \frac{T_{cog}(d_i) - T_{cog}(d_0)}{T_{cog}(d_0)} \end{aligned} \tag{6}$$

$Y(d_i)$ is the combined evaluation value of the solution set of each set of optimization variables; $T_{avg}(d_i)$, $T_{pkavg}(d_i)$, $Br_{\max}(d_i)$, and $T_{cog}(d_i)$ are the output torque, torque pulsation, peak air gap density, and cogging torque magnitude corresponding to each set of optimization variable solution set, respectively. $T_{avg}(d_0)$, $T_{pkavg}(d_0)$, $Br_{\max}(d_0)$, and $T_{cog}(d_0)$ are the output torque, torque pulsation, peak air-gap density, and cogging torque magnitude of the V-type PMM mentioned above, respectively.

Using the performance index of V-type PMM as a reference, quantify the degree of change in each optimization objective and assign values based on weighting coefficients to avoid situations where improving one optimization objective leads to a decline in others. This normalizes non-commensurable quantities and ultimately selects the optimal solution from the solution set.

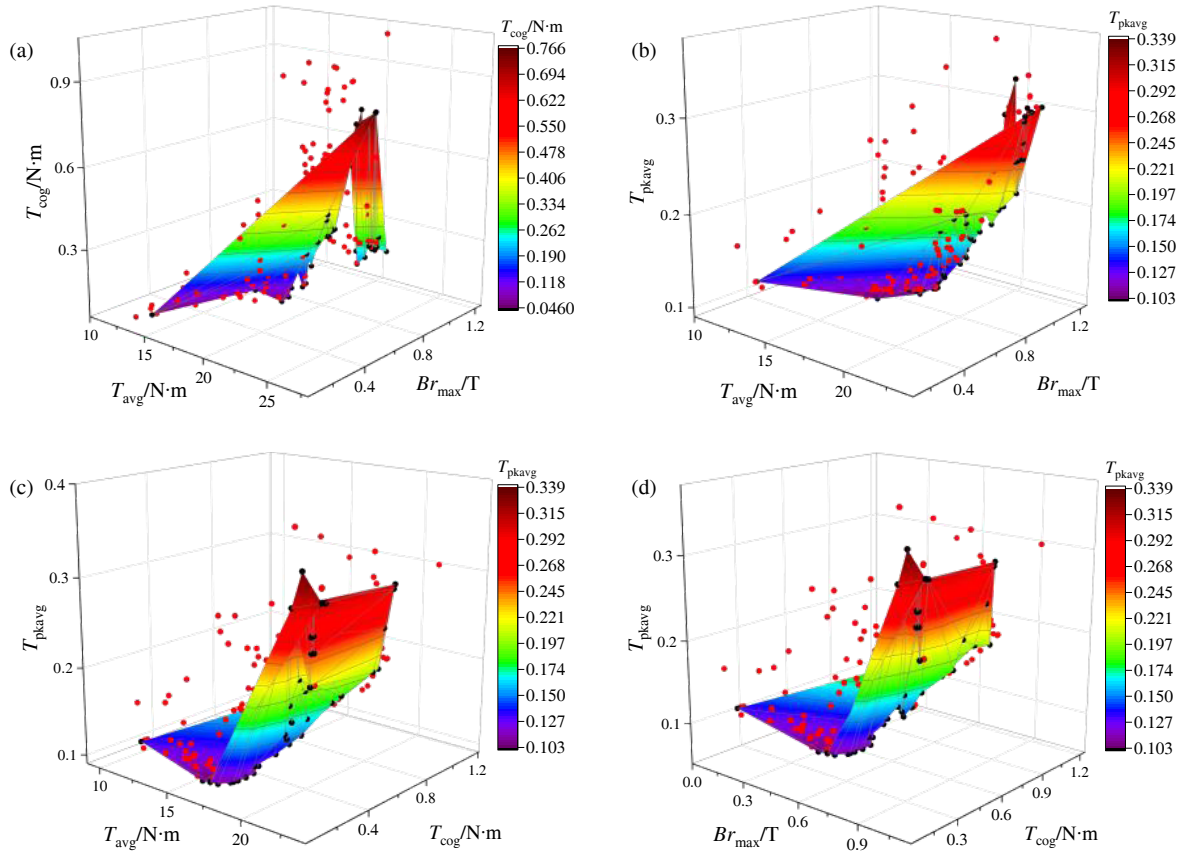

FIGURE 8. Distribution of Pareto frontiers for the solution set of high sensitivity optimization variables. (a) T_{avg}, $Br_{\max}$ and T_{cog}. (b) T_{avg}, $Br_{\max}$ and T_{pkavg}. (c) T_{avg}, T_{cog} and T_{pkavg}. (d) $Br_{\max}$, T_{cog} and T_{pkavg}.

TABLE 6. Partial optimization variables solution set, solution set composite rating values and rankings.

Serial number	a_2/ mm	α/°	b_2/ mm	β/°	T_{avg}/ N· m	$Br_{\max}$ /T	T_{cog}/ N· m	T_{pkavg}	$Y(d_i)$	rankings
44	8.27	79.38	6.10	111.96	19.12	0.829	0.351	0.1339	0.267	1
53	8.42	76.31	6.94	92.40	21.81	0.993	0.519	0.2593	0.220	28
71	8.39	79.02	6.87	89.83	22.12	1.010	0.403	0.2816	0.212	33
78	8.26	79.38	6.17	106.27	18.93	0.807	0.369	0.1259	0.264	3
79	6.33	71.85	5.02	103.93	12.83	0.260	0.263	0.1390	−0.005	49
...	...	...	...	...	...	...	...	...		
192	8.14	78.50	6.35	95.48	19.91	0.859	0.382	0.1849	0.232	21
195	8.39	79.34	6.84	90.43	22.02	1.005	0.398	0.2735	0.219	30
196	8.27	79.55	6.33	106.56	19.27	0.832	0.403	0.1363	0.258	5
198	8.39	79.17	6.82	86.46	22.32	1.020	0.396	0.3219	0.179	45
199	8.43	78.53	6.36	90.75	20.78	0.931	0.374	0.2476	0.208	35

The identified 49 groups of optimized variable solution sets were brought into the above equation, and the composite evaluation value of each group of optimized variable solution sets was calculated and ranked. Some of the optimized variable solution sets, the composite evaluation value of each group of optimized variable solution sets obtained from the calculations, and the rankings are shown in Table 6.

As can be seen from Table 6, among the 49 groups of optimization variables solution set, the 1st group of optimization variables solution set with serial number 44 has the highest comprehensive evaluation value. Taking into account the machining accuracy of the motor and machining difficulty and other issues, the 1st group of optimization variables solution set is rounded, and the parameters of each optimization variable after rounding are shown in Table 7.

3. MOTOR PERFORMANCE COMPARISON

The optimized completed ASLREPMM is compared with the V-type PMM as a reference in terms of cogging torque, out-

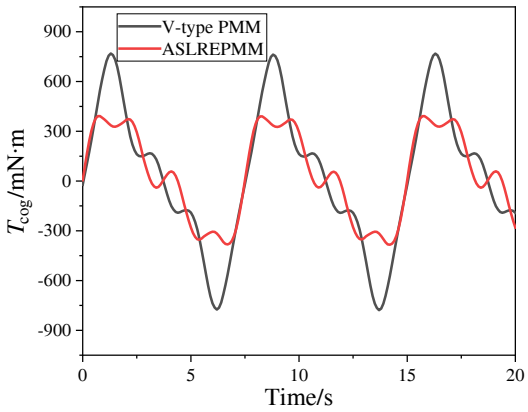

FIGURE 9. Comparison chart of cogging torque.

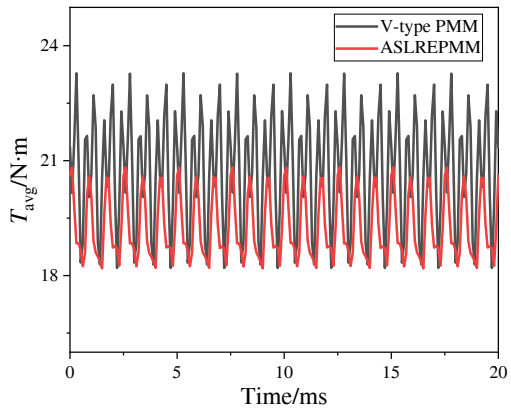

FIGURE 10. Output torque comparison chart.

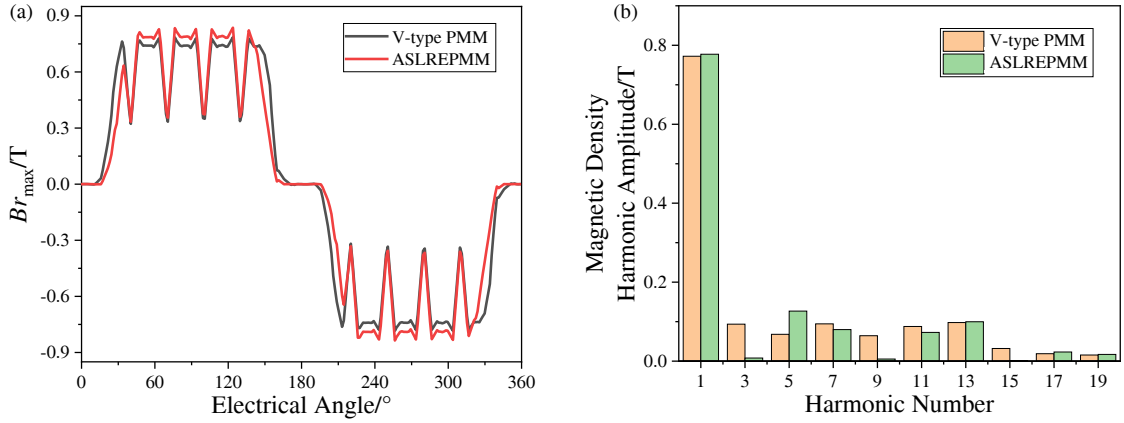

FIGURE 11. Comparison of air-gap magnetic density. (a) Comparison of air-gap magnetic density waveforms. (b) Comparison of magnetic density harmonic.

TABLE 7. Parameters of each optimization variable after rounding.

Variable	a_2/mm	α/°	b_2/mm	β/°
Before rounding	8.27	79.38	6.10	111.96
After rounding	8.3	79.4	6.10	112.0

put torque, torque pulsation with peak air-gap magnetism, and waveform aberration rate, in which the cogging torque, output torque, and air-gap magnetism comparison plots are shown in Fig. 9, Fig. 10, and Fig. 11, respectively.

As can be seen in Fig. 9, the cogging torque of the V-type PMM used as a reference is 778.2 mN·m, and the cogging torque of the optimized and completed ASLREPMM decreases significantly by 49.67% to 391.7 mN·m. From Fig. 10, it can be seen that the output torque of the V-type PMM used as a reference is higher at 20.77 N·m, and the output torque of the optimized asymmetrically ASLREPMM is lower at 19.26 N·m. The torque pulsation of the ASLREPMM is lower at 13.70%, which is a decrease of 10.77% in comparison with the torque pulsation of the V-type PMM. The results show that the ASLREPMM has lower cogging torque and torque pulsation, and although the output torque is slightly reduced, it can still satisfy the output demand of electric vehicles.

From Fig. 11(a), it can be seen that the ASLREPMM has higher peak air-gap density and more sinusoidal air-gap density waveforms than the V-type PMM, with the peak air-gap density increasing from 0.786 T to 0.837 T and the waveform distortion rate decreasing from 27.58% to 25.29%. From Fig. 11(b), it can be seen that the magnitude of the magnetically dense fundamental wave increases, and the magnitude of the 3rd, 7th, 9th, 11th, and 15th harmonics decreases significantly for the ASLREPMM.

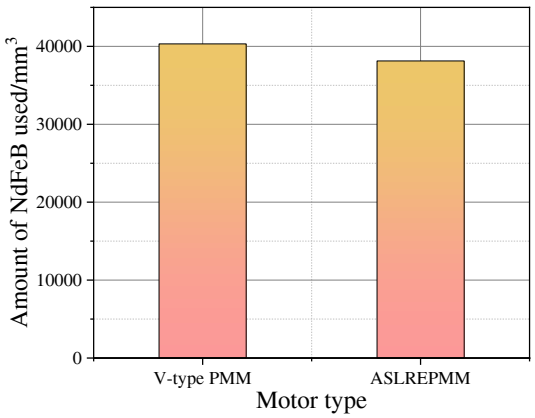

FIGURE 12. Comparison of NdFeB material usage.

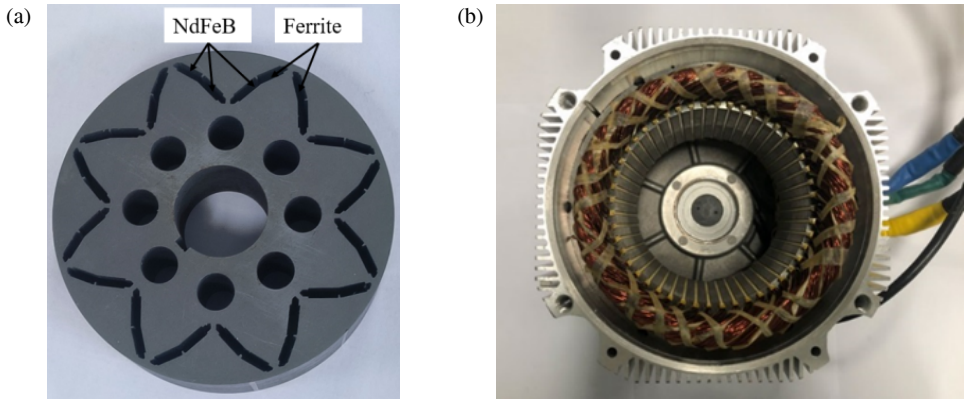

FIGURE 13. Sample machine composition. (a) Rotor core. (b) Stator assembly.

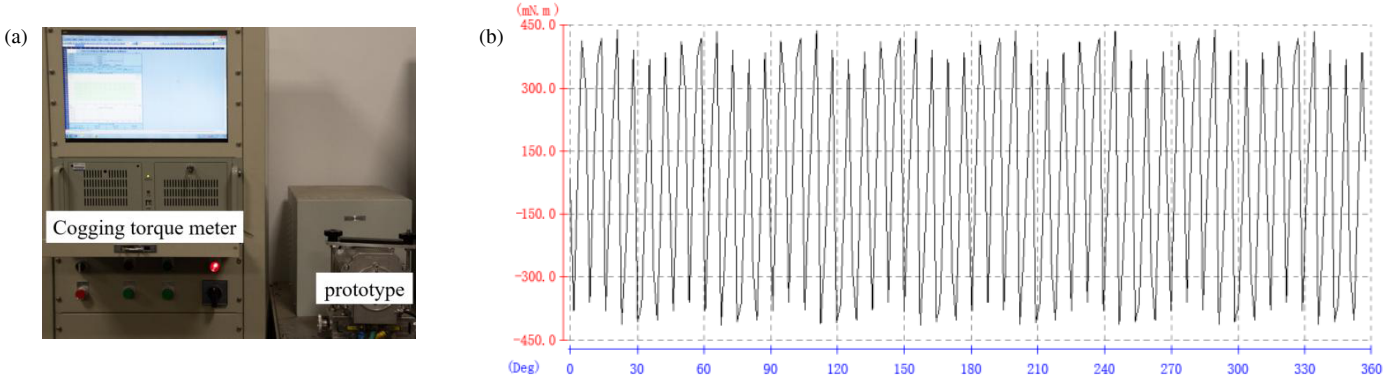

FIGURE 14. Cogging torque test. (a) Cogging torque test rig. (b) Mechanical properties test rig.

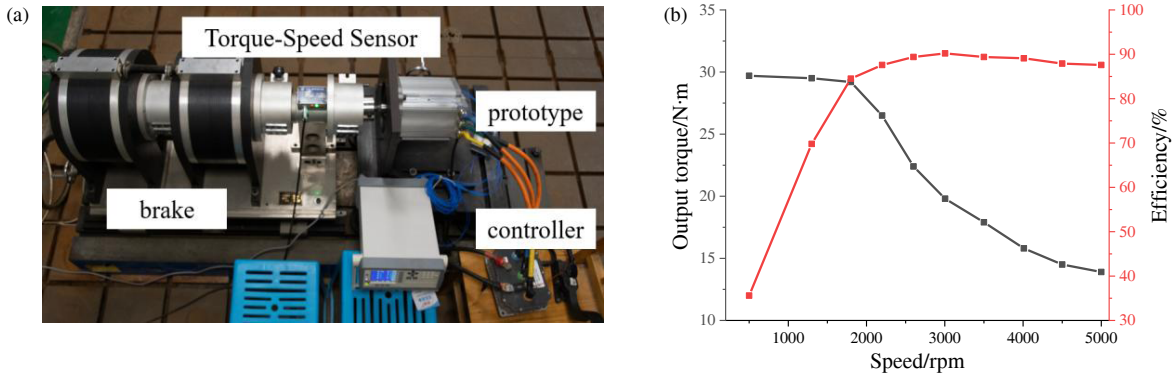

FIGURE 15. Motor mechanical characteristics test. (a) Testing platform for mechanical characteristics. (b) Mechanical property test result.

The NdFeB material usage of the ASLREPMM after completion of the optimization is compared with the NdFeB material usage of the V-type PMM, and the comparison graph is shown in Fig. 12.

As can be seen from Fig. 12, compared with the total NdFeB usage of 40320 mm^3 for the V-type PMM, the NdFeB usage of the optimized ASLREPMM is 38136 mm^3, with a reduction of NdFeB usage by 2184 mm^3, and the rare-earth usage is only 94.58% of the V-type PMM, which results in the reduction of the cost of the motor rare-earth material usage, and contributes to the lowering of the motor manufacturing cost.

4. EXPERIMENTAL VALIDATION

In order to further verify the electromagnetic characteristics of the proposed ASLREPMM and the validity of the optimization analysis, a prototype was fabricated, and the rotor core and stator assembly of the ASLREPMM are shown in Fig. 13.

The cogging torque test and mechanical characteristic test are carried out on the prototype, and the test results of the cogging torque test platform and cogging torque are shown in Fig. 14. The mechanical characteristics of the motor test platform and test results are shown in Fig. 15.

As can be seen from Fig. 14, the peak value of the cogging torque test result is 415.6 mN·m, which is slightly higher than the simulation result of 391.7 mN·m. Due to the experimental apparatus and motor assembly conditions, the test error is unavoidable, but the error is within the permissible range, which verifies the validity of the ASLREPMM. As can be seen from Fig. 15, the motor output torque at the rated speed measured in the test is 19.8 N·m, and the maximum efficiency is 90.4%. The maximum speed of the motor can be up to 5000 rpm, which meets the performance requirements of electric vehicles for the motor with large output torque and a wide speed regulation range.

5. CONCLUSION

In order to reduce the use of rare-earth material NdFeB and improve the electromagnetic performance of the motor, this paper proposes an ASLREPMM, through the multi-objective optimization of the motor parameters and prototyping and experimental validation of the completed optimized motor, and the following conclusions can be drawn:

(1) After the ASLREPMM uses the method of sensitivity analysis to determine the optimization variables with higher sensitivity to the optimization objectives and stratifies the optimization variables, the optimization variable parameters involved in the multi-objective optimization are reduced; the optimization time is reduced; and the efficiency is improved.

(2) Compared with the V-type PMM, the cogging torque and torque pulsation of the motor are reduced by 49.67% and 10.77%, respectively, and the sinusoidal property and peak value of the air-gap magnetic density waveform are improved by 2.29% and 0.051 T, respectively, with the use of segmented poles and arranged in an asymmetric form of the less rare earth PM motor.

(3) Comparing the NdFeB material usage, the NdFeB usage of the ASLREPMM is only 94.58% of the NdFeB usage of the V-type PM motor, and the NdFeB material usage is reduced by 2184 mm^3. The motor manufacturing cost is reduced.

REFERENCES

[1] El-Refaie, A., T. Raminosoa, P. Reddy, S. Galioto, D. Pan, K. Grace, J. Alexander, and K.-K. Huh, "Comparison of traction motors that reduce or eliminate rare-earth materials," *IET Electrical Systems in Transportation*, Vol. 7, No. 3, 207–214, 2017.

[2] Jun, C.-S. and B.-I. Kwon, "Performance comparison of a spoke-type PM motor with different permanent magnet shapes and the same magnet volume," *IET Electric Power Applications*, Vol. 11, No. 7, 1196–1204, 2017.

[3] Hu, W., X. Zhang, Y. Lei, Q. Du, L. Shi, and G. Liu, "Analytical model of air-gap field in hybrid excitation and interior permanent magnet machine for electric logistics vehicles," *IEEE Access*, Vol. 8, 148 237–148 249, 2020.

[4] Mohamed, M. Y., M. Fawzi, A. Kalas, A. S. Abdel-Khalik, S. Ahmed, and A. Refaat, "Optimized design of a fault-tolerant 12-slot/10-pole six-phase surface permanent magnet motor with asymmetrical winding configuration for electric vehicles," *Alexandria Engineering Journal*, Vol. 110, 527–539, 2025.

[5] Yang, Y., Q. He, C. Fu, S. Liao, and P. Tan, "Efficiency improvement of permanent magnet synchronous motor for electric vehicles," *Energy*, Vol. 213, 118859, 2020.

[6] Hefny, H., B. S. Yilmaz, D. Al-Ani, R. Z. Haddad, A. Emadi, and B. Bilgin, "Thermal modeling of an interior permanent magnet synchronous motor for an electric vehicle application," in *2024 IEEE Transportation Electrification Conference and Expo (ITEC)*, 1–6, Chicago, IL, USA, Jun. 2024.

[7] Wang, W., R. Fu, and Y. Fan, "Electromagnetic parameters matching of permanent magnet synchronous motor for hybrid electric vehicles," *IFAC-PapersOnLine*, Vol. 51, No. 31, 407–414, 2018.

[8] Jani, S. N. and J. G. Jamnani, "Performance analysis and comparison of PM-Assisted synchronous reluctance motor with ferrites and Rare-earth magnet materials," *Materials Today: Proceedings*, Vol. 62, 7162–7167, 2022.

[9] Nagarajan, V. S., V. Rajini, G. S. Mukundharajan, M. Barathkumar, and T. V. L. Vyshnavi, "Comparative evaluation of different permanent magnet materials for spoke interior permanent magnet motor suitable for automotive application," *Materials Today: Proceedings*, 2023.

[10] Nakamura, H., "The current and future status of rare earth permanent magnets," *Scripta Materialia*, Vol. 154, 273–276, 2018.

[11] Gu, A., M. Yang, X. Liu, L. Fu, C. Pang, and Y. Ren, "A research and optimization of a novel less-rare earth permanent magnet synchronous motor," in *2022 IEEE 9th International Conference on Power Electronics Systems and Applications (PESA)*, 1–6, Hong Kong, Sep. 2022.

[12] Wang, W., L. Fu, S. Wang, L. Zhu, Y. Liu, and J. Wei, "Research on magnetic circuit and electromagnetic performance of combined-pole less-rare-earth permanent-magnet synchronous machine used for fully electric unmanned aerial vehicle," in *2023 IEEE Transportation Electrification Conference and Expo, Asia-Pacific (ITEC Asia-Pacific)*, 1–6, Chiang Mai, Thailand, Nov. 2023.

[13] Lv, B., L. Shi, L. Li, K. Liu, and J. Jing, "Performance analysis of asymmetrical less-rare-earth permanent magnet motor for electric vehicle," *IET Electrical Systems in Transportation*, Vol. 12, No. 1, 36–48, 2022.

[14] Zhu, X., W. Wu, L. Quan, Z. Xiang, and W. Gu, "Design and multi-objective stratified optimization of a less-rare-earth hybrid permanent magnets motor with high torque density and low cost," *IEEE Transactions on Energy Conversion*, Vol. 34, No. 3, 1178–1189, 2018.

[15] Cai, T., Y. Chen, and J. Zhuang, "Hierarchical multi-objective optimization analysis of rare-earth asymmetric permanent magnet motor," *Micro Motor*, Vol. 54, No. 03, 14–19, 2021.

[16] Sheng, Z. and D. Wang, "Design and analysis of a kind of rotor ironless high torque density machine using Alnico magnet," *IET Electric Power Applications*, Vol. 14, No. 8, 1469–1479, 2020.

[17] Zeng, X., L. Quan, X. Zhu, L. Xu, and F. Liu, "Investigation of an asymmetrical rotor hybrid permanent magnet motor for approaching maximum output torque," *IEEE Transactions on Applied Superconductivity*, Vol. 29, No. 2, 1–4, 2019.